PNAS RESEARCH ARTICLE | ENVIRONMENTAL SCIENCES OPEN ACCESS

Dynamic treeline and cryosphere response to pronounced mid-Holocene climatic variability in the US Rocky Mountains

Gregory T. Pederson[a,1], Daniel Stahle[a,b], David B. McWethy[b], Matthew Toohey[c], Johann Jungclaus[d], Craig Lee[e], Justin Martin[a], Mio Alt[b], Nickolas Kichas[a], Nathan Chellman[f], Joseph R. McConnell[f], and Cathy Whitlock[b,1]

Affiliations are included on p. 10.

Contributed by Cathy Whitlock; received June 20, 2024; accepted November 27, 2024; reviewed by Andy G. Bunn and Bryan N. Shuman

Climate-driven changes in high-elevation forest distribution and reductions in snow and ice cover have major implications for ecosystems and global water security. In the Greater Yellowstone Ecosystem of the Rocky Mountains (United States), recent melting of a high-elevation (3,091 m asl) ice patch exposed a mature stand of whitebark pine (*Pinus albicaulis*) trees, located ~180 m in elevation above modern treeline, that date to the mid-Holocene (c. 5,950 to 5,440 cal y BP). Here, we used this subfossil wood record to develop tree-ring-based temperature estimates for the upper-elevation climate conditions that resulted in ancient forest establishment and growth and the subsequent regional ice-patch growth and downslope shift of treeline. Results suggest that mid-Holocene forest establishment and growth occurred under warm-season (May-Oct) mean temperatures of 6.2 °C (±0.2 °C), until a multicentury cooling anomaly suppressed temperatures below 5.8 °C, resulting in stand mortality by c. 5,440 y BP. Transient climate model simulations indicate that regional cooling was driven by changes in summer insolation and Northern Hemisphere volcanism. The initial cooling event was followed centuries later (c. 5,100 y BP) by sustained Icelandic volcanic eruptions that forced a centennial-scale 1.0 °C summer cooling anomaly and led to rapid ice-patch growth and preservation of the trees. With recent warming (c. 2000–2020 CE), warm-season temperatures now equal and will soon exceed those of the mid-Holocene period of high treeline. It is likely that perennial ice cover will again disappear from the region, and treeline may expand upslope so long as plant-available moisture and disturbance are not limiting.

whitebark pine | cyrosphere | climate change | treeline | Yellowstone

Significance

Recent warming has decreased snow and ice cover and increased the elevation of most subalpine treelines around the world. A mid-Holocene (c. 5,950 to 5,440 cal y BP) whitebark pine forest preserved within a perennial ice patch in the Greater Yellowstone Ecosystem provides insights into the consequences of past climate change and ecosystem dynamics. Mid-Holocene treeline expanded ~180 m above its modern elevation when warm-season temperatures were similar to mid-to-late-20th-century conditions. Treeline elevation was subsequently lowered due to periods of cooling related to increased volcanism, but primarily from declining summer insolation during the late Holocene. As current ice-patch temperatures exceed the warmest mid-Holocene conditions, we expect regional loss of ice patches and possibly renewed upslope treeline expansion.

Recent warming across the western United States and globally has substantially transformed mountain ecosystems through reductions in snow and ice (1–4), increased fire and insect disturbance (5–7), and altered species ranges (8, 9). Globally, high-elevation treeline exhibits a strong sensitivity to temperature (10–12), responding through changes in elevation as well as growth and density (13). The thermal sensitivity of global treeline elevations, as first documented by Hermes (14) and subsequently Körner (10), is strongly reflected by the close correspondence to global snowline elevations and a narrow growing-season temperature range of 5.5 to 7.5 °C associated with treeline elevations irrespective of growing-season length (ranging from 2.5 mo at high latitudes to 12 mo in the tropics and subtropics). Northern Hemisphere treelines at mid-latitudes (30°N to 50°N), in particular, are sensitive to temperatures over a five- to seven-month warm season (10), specifically those of "diffuse" form that are characterized by a gradual upslope decrease in tree height and density (13). At local to regional scales, however, other topographic and climate factors, such as winter temperatures, snowpack, and moisture availability, may be most limiting and determine whether a particular treeline is stable or dynamic (i.e., actively advancing or retreating), as well as its specific spatial pattern or "form" (e.g., diffuse, abrupt, island, and krummholz treeline) (15–19). Variations in local conditions likely explain why recent warming documented at approximately 70% of treelines globally only resulted in ~50% exhibiting upslope advances (13, 15). Although the rapid rates of warming projected for high elevations (20) in the future may promote treeline expansion in many locations, the complexity of factors that amplify or inhibit treeline establishment poses challenges for predicting specific ecological dynamics. Investigating long-term ecosystem responses to a range of high-elevation climate conditions over the Holocene (c. 12,000 y BP to present) facilitates our ability to assess current and future treeline dynamics, snow and ice cover, and the associated implications for high-elevation sourced water resources.

Perennial ice patches are a widespread and unique land cover found at most latitudes that provide new information on past high-elevation ecosystem dynamics, climate, and

Author contributions: G.T.P., D.B.M., M.A., J.R.M., and C.W. designed research; G.T.P. and D.S. performed research; M.T. and J.J. contributed new reagents/analytic tools; G.T.P., D.S., and N.K. analyzed data; G.T.P., D.S., D.B.M., C.L., M.A., N.C., and J.R.M. collected field data and contributed data; and G.T.P., D.S., D.B.M., M.T., J.J., C.L., J.M., M.A., N.K., N.C., J.R.M., and C.W. wrote the paper.

Reviewers: A.G.B., Western Washington University; and B.N.S., University of Wyoming.

The authors declare no competing interest.

[1]To whom correspondence may be addressed. Email: gpederson@usgs.gov or whitlock@montana.edu.

This article contains supporting information online at https://www.pnas.org/lookup/suppl/doi:10.1073/pnas.2412162121/-/DCSupplemental.

Published December 30, 2024.

even human lifeways (21–24). Unlike glaciers, ice patches do not flow, and until recently, they exhibited slow, near-continuous ice accumulation, allowing preservation of deposited materials such as pollen, charcoal, and macrofossils within their frozen layers, as well as biological materials beneath the stable ice mass that predate ice establishment (21, 22). Across the Greater Yellowstone Ecosystem (Fig. 1), ice patches are distributed from near-modern treeline to the highest elevations, and radiocarbon dating of organic matter from ice cores and remnant wood collected at numerous ice-patch locations indicate that some initiated growth and persisted during the early- to mid-Holocene warm period (10,500–6,000 y BP) (21–24). Recent warming-driven ice melt (25, 26) has exposed archeological and biological materials at the margins and threatens the loss of the chronologically ordered organic layers contained within the ice patches. Currently, these ice-patch archives provide Holocene-length records of high-elevation climate and ecosystem change that are rare or absent from other interior continental proxies.

During a field survey, over 30 well-preserved large trees (>25 cm diameter) were found melting out of an ice patch (named "TOL," elev. ~3,091 m asl) on the Beartooth Plateau in the northeastern corner of the Greater Yellowstone Ecosystem. The site is located ~150 to 180 m above a diffuse modern treeline (named "TAL," elev. ~2,908 m asl) (Fig. 1 and *SI Appendix*, Supporting Information Text S1; hereafter, "S" signifies Supporting Information) (24). The subfossil trees at the ice patch (TOL) were identified as whitebark pine (*Pinus albicaulis*) based on their wood anatomy and proximity to downslope whitebark pine forests (27). Radiocarbon dates obtained from bulk-wood samples suggest the ancient stand persisted over multiple centuries in the mid-Holocene, with median calibrated dates centered around 5,500 y BP. The presence of the stand raises important questions about the climate conditions that led to tree establishment, demise, and preservation within the ice patch. Whitebark pine trees growing at or near upper treeline today exhibit growth-climate relationships predominantly controlled by warm-season temperature, even during periods of drought, and often across multiple growing seasons due to lagged climate and physiological processes (e.g., carbon storage) (28, 29). This temperature-growth relationship is shared with other five-needle pines, such as bristlecone pine (*Pinus longaeva*), growing at or near upper treeline, and results in the retention of a strong temperature signal at decadal to multicentennial timescales (30–32). The extraordinary quality of wood preservation at the TOL ice-patch site provides an opportunity to generate a multicentury, mid-Holocene record of high-elevation temperature during the life of the forest stand, and to elucidate

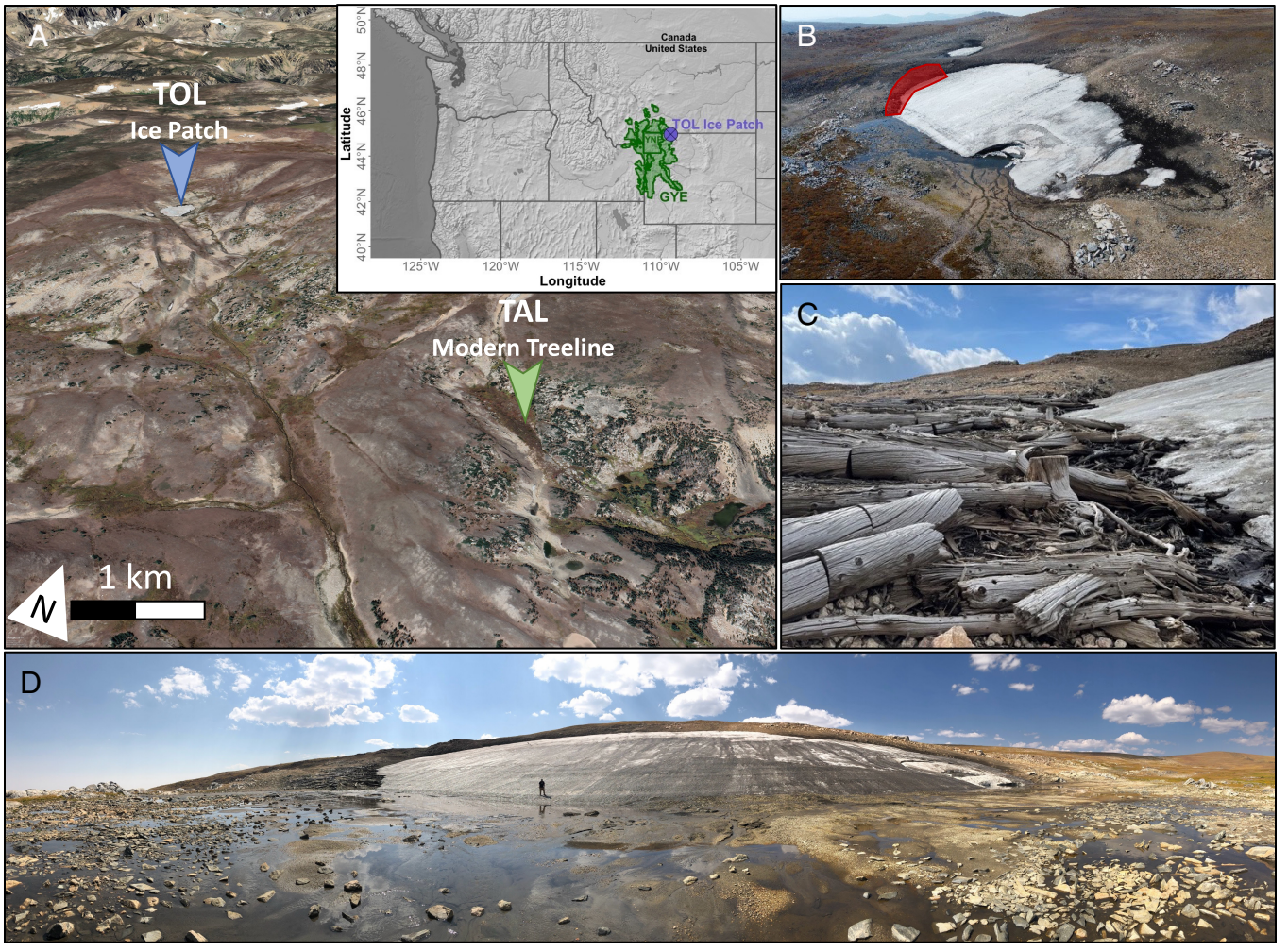

Fig. 1. (*A*) Location of the ice patch (TOL) with the mid-Holocene whitebark pine stand relative to the modern treeline site (TAL). The map inset shows the approximate location of the study site (purple circle) within the Greater Yellowstone Ecosystem (GYE; green polygon) (Basemaps from Natural Earth and Google Earth courtesy of Maxar Technologies). (*B*) Aerial image showing the ice patch and ice-patch margin where the whitebark pine trees were sampled (red polygon) (photo by Joe McConnell, captured 6 Sep 2021). (*C*) The sampled subfossil whitebark pine trees along the margin of the TOL ice patch (photo by Daniel Stahle). (*D*) Panoramic view of the forefield of the ice patch showing the exposed ice surface from extensive melt during the 2024 ablation season (photo by Gregory Pederson, captured 8 Sep 2024).

the climate conditions that contributed to the stand's demise and subsequent growth of the ice patch.

At a nearby (within ~5 km) ice patch (named "TL1," elev. ~3,145 m asl), well-dated ice cores have provided both a cool-season temperature and moisture record for the last 10,400 y along with a paleobotanical record of treeline dynamics (21, 22). The paleoclimate record was interpreted from the ice-derived water isotope ($\delta^{18}O$) chronology and estimated ice accumulation rates between radiocarbon-dated organic layers. Pollen and plant macrofossils within the ice-patch organic layers and at a nearby wetland were used to reconstruct the vegetation history. The TL1 records indicate that, during the early Holocene (9,000–6,500 y BP), tundra vegetation was more widespread than at present due to dry conditions and potentially cold winters. The maximum upslope forest cover expansion at the TL1 ice patch was inferred by Alt et al. (21) to have occurred during the mid-Holocene (6,500–4,200 y BP), when increased plant-available moisture was attributed to cooler warm-season and wetter cool-season conditions than before. During the late Holocene (after 4,200 y BP), cool summers reduced forest cover and shifted treeline downslope to near-modern elevations (21).

Here, we use the subfossil whitebark pine tree-ring record recovered from the TOL ice patch to compare the recent magnitude of high-elevation warming with mid-Holocene conditions and to understand the late-Holocene changes in climate that resulted in regional ice-patch growth and lowered treeline elevation. We utilize the whitebark pine tree-ring record to infer mid-Holocene high-elevation temperature by 1) developing cross-dated ring-width chronologies for the ice-patch (TOL) and nearby modern-treeline site (TAL); 2) accurately dating the mid-Holocene floating chronology (TOL) using calibrated radiocarbon dates from individual growth rings in multiple trees; 3) establishing growth-climate relationships from the modern-treeline (TAL) chronology and historical snow and climate records; and 4) applying linear and nonlinear transfer functions based on modern growth-climate relationships to infer the climate conditions (predominantly at decadal to centennial timescales) that supported the growth of the subfossil whitebark pine stand. Additionally, we compare our tree-ring-based reconstruction with results from mid-Holocene-to-present transient climate model simulations (33, 34) to disentangle the climate forcings, seasonality, and sequence of events that led to the establishment and the eventual demise of the whitebark pine stand and to the rapid tree burial and preservation within the growing ice patch. The simulations carried out with the Max Planck Institute Earth System Model (MPI-ESM, *Materials and Methods*) apply a new global volcanic stratospheric sulfur dataset from Sigl et al. (35) and include the effects of changing greenhouse-gas concentrations, aerosols, landcover, and insolation on regional climate patterns and trends.

Results and Discussion

Radiocarbon Dating of the Ice-Patch Subfossil Whitebark Pine Chronology. Accurate calendar dating of the floating ice-patch (TOL) chronology (*SI Appendix*, Fig. S1*A* and Table S1) was achieved by first obtaining individual ^{14}C values and uncertainty ranges from eleven cross-dated and sampled annual growth rings and plotting these along the "IntCal20" calibration curve (Fig. 2*A* and *SI Appendix*, Table S2). The eleven dated rings were sampled from different growth years across the 512-year-long chronology, which allowed us to jointly use the radiocarbon dates to produce more accurate calibrated dates by wiggle-matching against the calibration curve. Median calibrated radiocarbon dates of the youngest and oldest individual rings suggest that the forest stand, at a minimum, spanned years 5,940 (5990–5910 2σ range) to 5,520 (5,578–5,479 2σ range) y BP (Fig. 2*A* and *SI Appendix*, Table S2). We further reduced the dating uncertainty of the chronology by regressing the median calibrated radiocarbon dates against the growth years of the eleven dated and sampled rings from within the floating chronology (Fig. 2*B*). Since cross-dated growth rings have annual dating accuracy, the linear relationship between samples jointly leveraged all the radiocarbon dates to estimate a more precise calibrated date for the chronology. The resulting calibrated date range for the floating ice-patch chronology spanned c. 5,950 to 5,440 cal y BP with the root-mean-squared error (RMSE) from the linear regression providing a conservative uncertainty estimate of ± 51 y (Fig. 2*B*). This chronology places the whitebark pine record within the mid-Holocene period of higher treeline inferred from the nearby TL1 site (21) and with ancient bristlecone pine treeline sites in the Great Basin of the southwestern United States (30, 31).

Mid-Holocene Temperature Reconstructions. Whitebark pine growth at treeline may be limited by a range of climatic controls (e.g., temperature and snowpack) across seasons and over multiple years (37). Comparison of growth characteristics and dominant frequencies of variability between the modern (TAL) and

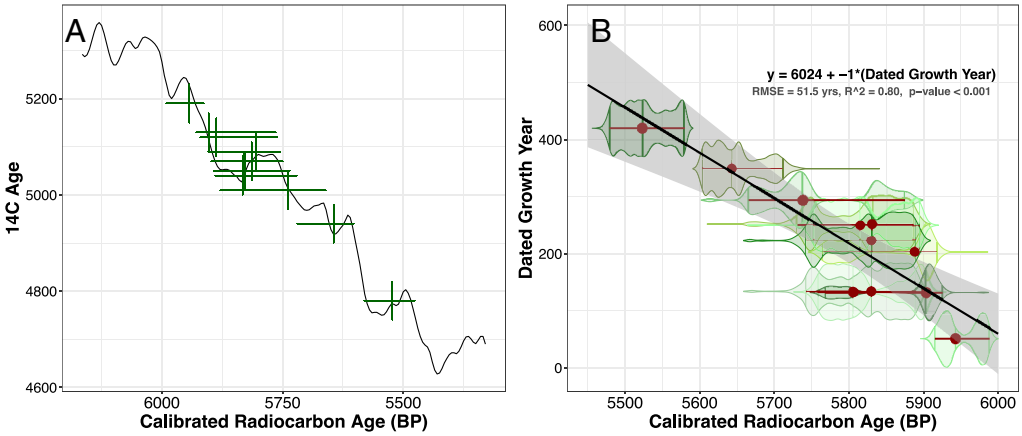

Fig. 2. (*A*) The individual dated annual growth-ring calibrated radiocarbon ages versus the ^{14}C ages and uncertainty range (green crosses) plotted along the "IntCal20" radiocarbon calibration curve (black line) (36). (*B*) Regression analysis establishing the accurate calibrated dates (shown in years B.P.) of the TOL whitebark pine chronology. Accurate dating was established using the linear relationship (black regression line bounded by gray 95% CI) between the calibrated median radiocarbon dates (red circles with 2σ uncertainty) from the radiocarbon age distributions (green violin plots) and the dated growth year assigned to the same cross-dated ring.

mid-Holocene (TOL) chronologies suggests the records exhibit similar interannual persistence and significant ($P < 0.1$) multidecadal- to centennial-scale variability consistent with temperature-limited growth (*SI Appendix*, Text S2 and Figs. S2–S4). Evaluation of the modern (1900–2018 CE) growth-climate response of whitebark pine at the TAL treeline site (Fig. 1*A* and *SI Appendix*, Fig. S1*B*) indicates primary control by warm-season (May–Oct) average temperature in current and prior years (*SI Appendix*, Text S2 and Figs. S5–S8). This multiyear growth-temperature relationship was the basis for reconstructing average warm-season to biennial (prior Jan–Oct; 22-mo span) temperature at the TOL ice patch.

Linear (MLR) and nonlinear (BRNN) transfer functions (Fig. 3 and *SI Appendix*, Fig. S9) were used to estimate temperatures from the subfossil wood at the ice patch (TOL) and bracket uncertainty in the reconstructed temperatures on the reasoning that predictions of past temperatures were partially based on extrapolation from the colder and slower growth end of the modern treeline (TAL) distribution (*SI Appendix*, Table S1 and Fig. S2). Over the calibration period (1900–2018 CE), both regression approaches exhibited highly similar results, with the biennial reconstructions producing more accurate predictions with smaller associated uncertainty (Fig. 3 and *SI Appendix*, Figs. S10–S12 and Tables S3 and S4 and Text S2). Similar results were evident for the mid-Holocene period with minor differences between methods shown, as expected, for the coldest estimated temperatures (Fig. 4 and *SI Appendix*, Figs. S13–S15). Nonetheless, both versions of the reconstructions show common low-frequency variation and trends in temperature. Though the biennial growth-temperature responses were statistically the most skillful, the strongest monthly-to-seasonal temperature correlations occurred during the warm seasons (*SI Appendix*, Figs. S5 and S7), suggesting that overall growth response and resulting seasonal reconstructions were weighted to reflect growing-season climate conditions. Additionally, the dominant low-frequency variability common to both chronologies (*SI Appendix*, Fig. S4) suggests that the records

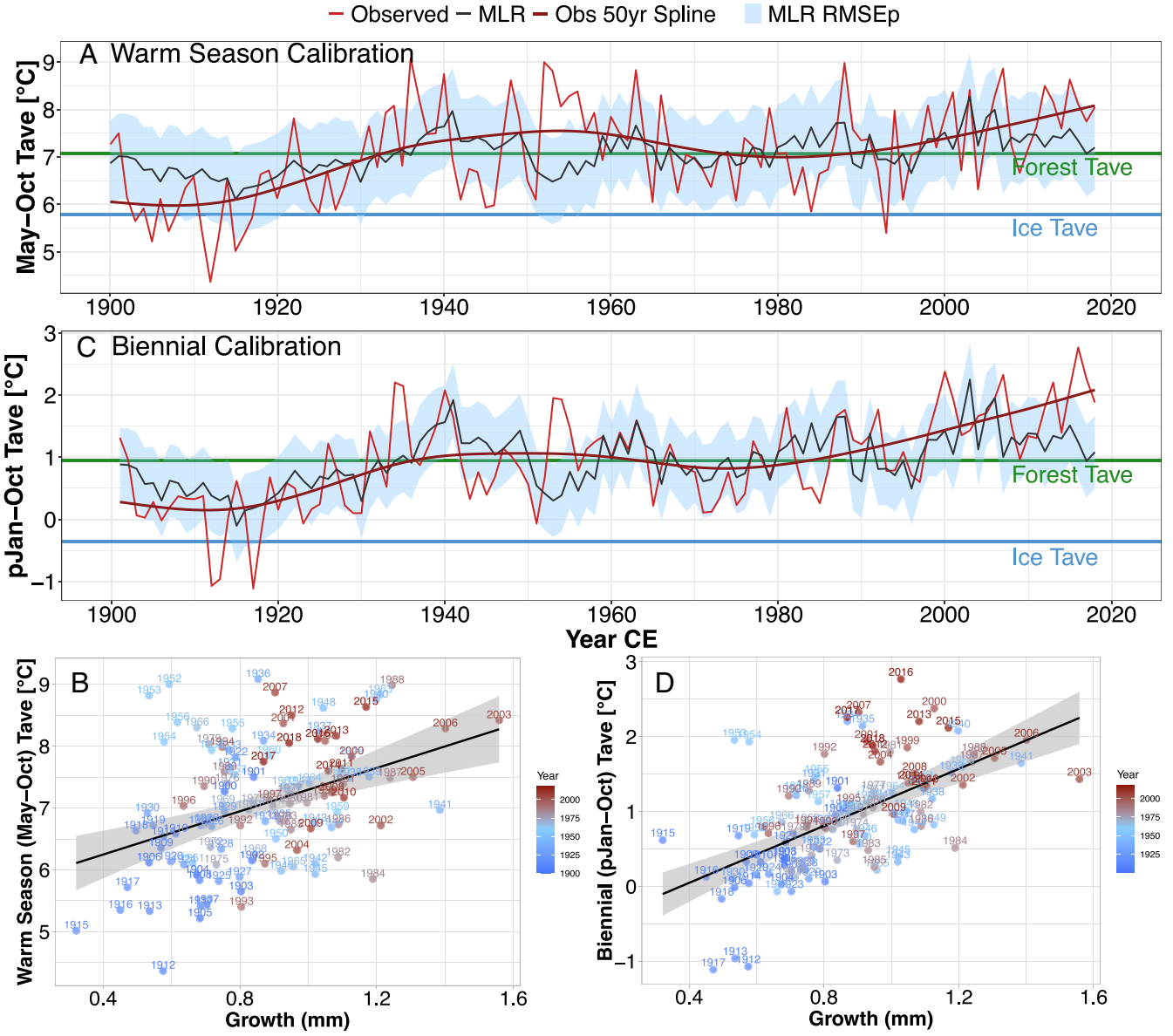

Fig. 3. Calibration of the average temperature (Tave) reconstructions based on linear (MLR) regression analysis for the (*A* and *B*) warm season (May–Oct) and (*C and D*) biennial period (prior Jan–Oct) over the 1900–2018 common interval. The reconstructions are bounded by the root-mean-squared error of the prediction (RMSEp) and the modern mean temperature for the period of record at the TOL ice-patch (blue line) and TAL modern-treeline site (green line) are shown for reference. The scatter plots (*C* and *D*) include the transfer function linear relationships (MLR) with 95% CI and are shown with years labeled and plotted on a color gradient reflecting recent decades of anomalously warm temperatures (red) corresponding with higher average growth.

retain the warm-season temperature signal mostly at decadal to multicentennial timescales, a result similar to that for bristlecone pine growing near treeline (30). Consequently, we focus our discussion primarily on the decadal- to centennial-scale changes in warm-season (May–Oct) and biennial (prior Jan–Oct) average temperature due to their role in governing treeline and ice dynamics and correspondingly greater statistical skill.

Substantial uncertainty exists in the mid-Holocene treeline temperature estimates and stems from multiple contributing sources, including: 1) the dating uncertainty of the floating ice-patch chronology (TOL); 2) the multiyear and predominately low-frequency growth-climate response; 3) determination of the actual mid-Holocene treeline elevation and associated cold zone of temperature-limited tree-growth (i.e., the relatively narrow elevational band of strong growth limitation from temperature, below which moisture becomes most limiting)- the TOL ice-patch trees only provide a minimum estimate; and 4) the potential confounding influence of persistent snowpack or possible presence of a reduced ice patch on the mid-Holocene forest microclimate. From the multiple methods employed herein, and the growth characteristics of the forest stand (*SI Appendix*, Text S1 and S2 and Figs. S2–S8), we minimized the dating and climate-growth uncertainties associated with the mid-Holocene temperature estimates. However, these relationships suggest that the temperature response of the trees was strongest at decadal to centennial timescales, and the resulting reconstructions are primarily a record of low-frequency temperature change. Thus, we argue the mean and range of reconstructed temperature estimates are most representative of the decadal- to centennial-scale seasonal temperature mean, and the root-mean-squared error from the reconstruction prediction (RMSEp) of withheld observed temperature values characterizes the range of interannual temperature variability. These relationships are shown in Fig. 3, where the reconstructed temperatures from the modern-treeline site (TAL) closely track the long-term observed temperature mean and trend, and the RMSEp bounds most of the range of observed annual temperature values.

The mid-Holocene temperature reconstructions span nearly five centuries, covering a period from c. 5,900 to 5,440 cal. y BP (Fig. 4 and *SI Appendix*, Figs. S13–S15) after omitting the early portion of the record where sample number falls below four individual trees (EPS < 0.85). Over the early half of the reconstructions (c. 5,900–5,650 y BP), temperatures varied by ~0.2 °C around an average warm-season mean of 6.2 °C (0.0 °C biennial mean), a temperature range that was conducive to, but suboptimal for, tree growth (11). A 200-y-long period of cooling began after c. 5,650 y BP and ended in conditions approximately equivalent to early- to mid-20th-century average temperatures at the ice patch (Fig. 4). Over recent decades (2000–2020 CE), observed and tree-ring estimated temperatures at the ice patch equaled and exceeded the warmest reconstructed temperatures of the mid-Holocene (Fig. 4).

Climate Controls on Mid-Holocene Treeline and Ice-Patch Dynamics. The warm-season and biennial average temperature reconstructions at the ice patch (TOL) indicate that temperature was the primary control limiting tree growth and persistence of the whitebark pine forest stand (Fig. 4 and *SI Appendix*, Figs. S13-S15). The estimated warm-season temperature mean of 6.2 ± 0.2 °C from 5,900 to 5,650 y BP falls well within Körner's estimated 5.5 to 7.5 °C growing-season

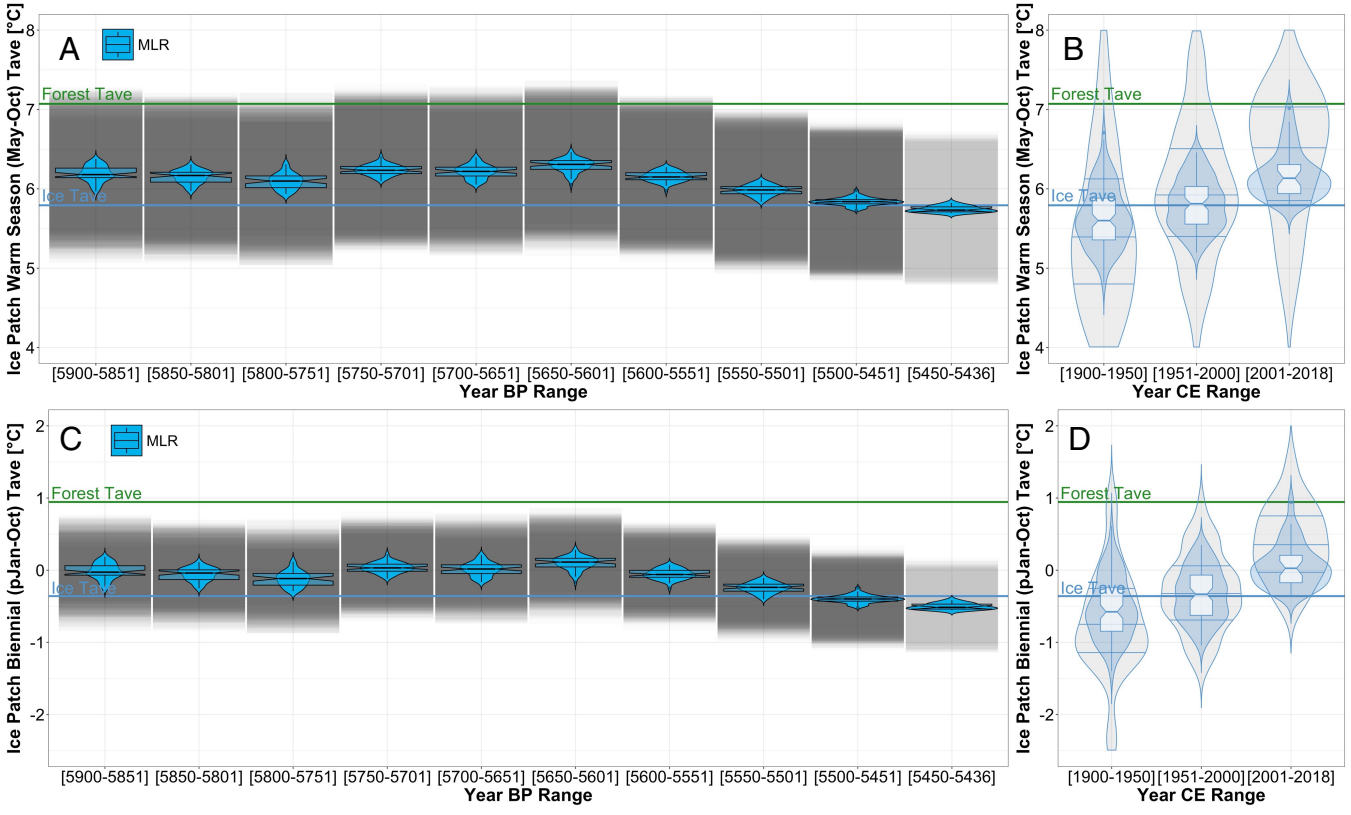

Fig. 4. Mid-Holocene climate compared to modern conditions at the TOL ice-patch site, based on 50-y (binned) reconstructed average temperature (Tave) for the (*A and B*) warm-season (May-Oct) and (*C and D*) biennial (previous Jan–Oct) reconstructions. Box and violin plots of the linear (MLR; blue) temperature reconstructions are shown bounded by the root-mean-squared error of the prediction (gray boxes) representing the range of interannual temperature variability*. In panels *B* and *D*, observed 50-y average temperature bins are plotted as light gray violin plots (with horizontal lines indicating the 25, 50, and 75% interquartile range) along with the temperature estimates from the TAL modern reconstructions (blue violin and light blue notched box plots). The mean temperature for the modern record (1900–2020 CE) at the TOL ice patch (blue line) and TAL forest site (green line) are shown for reference. *Note, the gray prediction error bounding boxes for period 5450–5436 y BP appear lighter because only 14 y of data are contained within the bin.

temperature range associated with modern global treeline positions and nearly equals the global average of 6.4 ± 0.7 °C (11, 12). It also suggests the trees were growing within or near the treeline cold zone of temperature-limited growth (± 50 to 150 m) (19, 31, 38). However, if a small ice-patch remnant cooled the proximal forest temperatures, the actual treeline elevation may have been higher. A subsequent 200-y-long period of cooling after c. 5,650 y BP reduced mean warm-season and biennial temperatures by ~0.4 °C, and led to the cessation of growth and demise of the whitebark pine stand by c. 5,440 y BP. During this period, mean warm-season temperatures were estimated to be ~5.8 °C, and the inferred range of interannual temperatures frequently exceeded the 5.5 °C lower threshold for tree growth (Fig. 4). Tree canopies at treeline are tightly coupled to atmospheric temperatures, and the root zone beneath a closed canopy forest is much colder than under surrounding low-stature vegetation due to reduced solar heat flux (10, 11). These factors result in trees at treeline frequently experiencing reduced or blocked meristem and root growth, and these conditions have been shown to occur globally when daily air and below-canopy soil temperatures fall below a temperature threshold of 6 to 7 °C even though photosynthesis rates are sufficient for growth (11). Thus, we infer that centuries-long cooling likely surpassed the temperature threshold required for growth and resulted in stand-wide growth-rate declines, increased tree mortality, and increased ice accretion at the ice patch. This cooling extended to high-elevation areas across the Greater Yellowstone Ecosystem, as evidenced by increased ice-accretion rates at TL1 (22), and the formation of new ice patches and glaciers in nivation hollows and other topographically suitable locations for ice accumulation (39). From the demise and subsequent lack of whitebark pine reestablishment at our study site, we estimate an average warm-season mortality temperature threshold of ~5.8 °C (–0.3 °C biennial) (Figs. 4 and 5 *A* and *C*).

Potential climate forcings underlying mid-Holocene cooling, treeline suppression, and ice-patch growth were investigated through

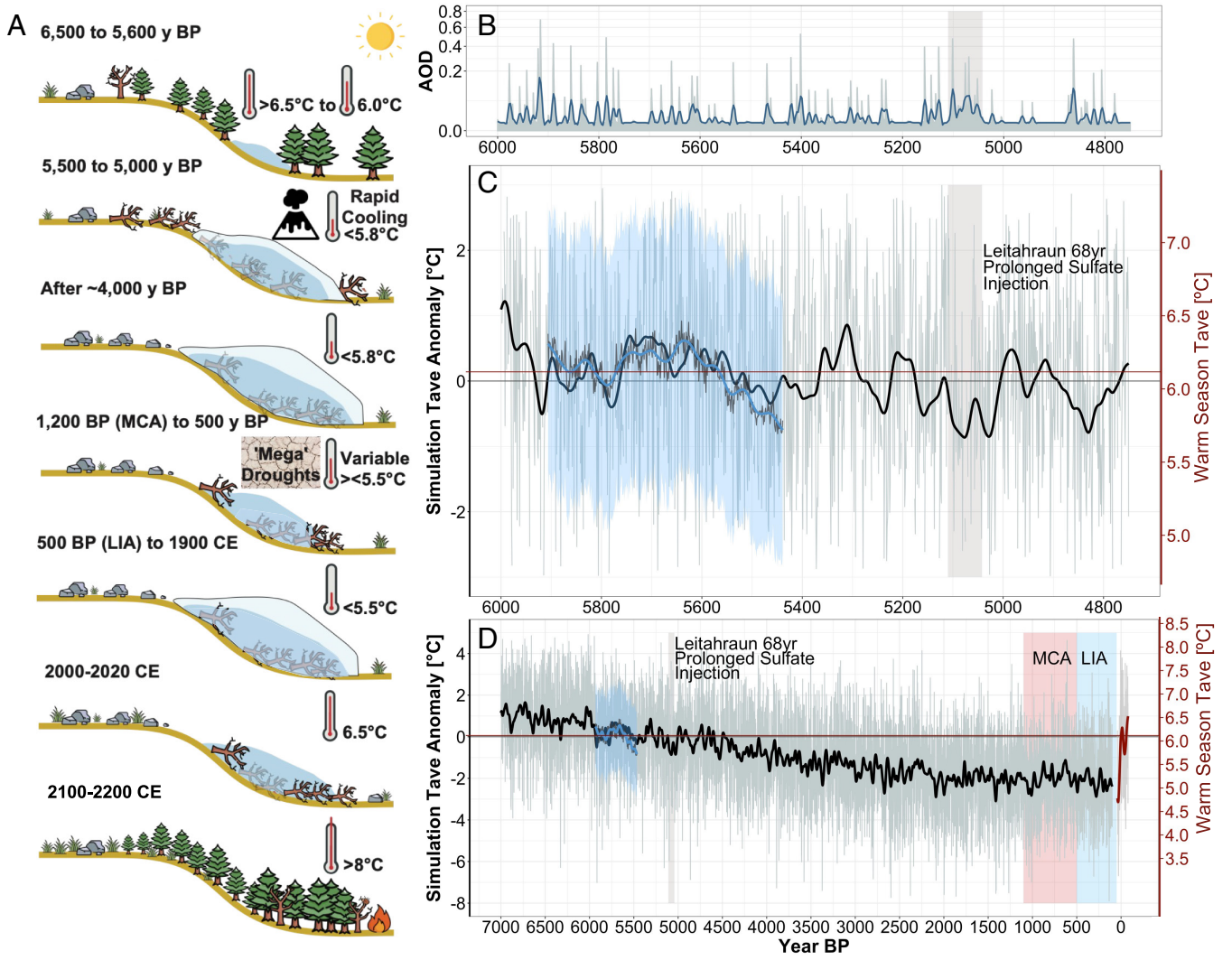

Fig. 5. (*A*) Conceptual illustration of changes in treeline elevation and ice-patch dynamics from the mid-Holocene to potential future at the TOL ice-patch site. The treeline and ice dynamics are driven by reconstructed, observed, and modeled changes in warm-season temperature represented by the thermometers. (*B*) Stratospheric Aerosol Optical Depth (AOD; annual values plotted with gray line are smoothed with a blue 50-y spline) representative of volcanic sulfate aerosols used in the transient Holocene climate model simulation for the 45°N latitude band (35). (*C*) Model simulated mid-Holocene average summer (Jun-Aug) temperature anomalies (gray lines are smoothed with black 50-y spline, left black y-axis) for the Greater Yellowstone Ecosystem compared with the ice-patch (TOL) warm-season (May-Oct) average temperature reconstruction (right red y-axis). The linear (MLR) reconstruction was smoothed with a blue 50-y spline and bounded in blue shading by the root-mean-squared error of prediction, which represents the range of annual temperature variability. The modeled temperature data are from a 2° × 2° grid cell located over the Greater Yellowstone Ecosystem and plotted as anomalies from the 6,000–4,500 y BP mean. (*D*) Same as C but showing the simulated mid-Holocene regional summer temperature declines up to 1850 CE, with the modern (1900–2020 CE) warm-season average temperature record at TOL plotted for reference (gray line smoothed with red 50-y spline) on the same axis as the reconstruction (right red y-axis). The Medieval Climate Anomaly (MCA) and the Little Ice Age (LIA) are labeled and highlighted with light red and light blue shading, respectively.

a comparison with simulations from a high-resolution, global transient climate model. For mid- to high-latitude regions north of 30°N, Bader et al. (40) simulated gradual mid-Holocene cooling in annual average temperatures that accelerated around 4,000 y BP. Most relevant to the Greater Yellowstone Ecosystem, a region of pronounced cooling developed over the western United States at this time that was driven by increasing Arctic summer sea-ice cover and decreasing summer high-latitude insolation (40). This mid-continental cooling event is also shown as a millennial-scale temperature decline beginning about 5,600 y BP in a pollen-based temperature reconstruction by Shuman and Marsicek (41), as well as in multiple independent proxies (42). In addition to the general cooling trend, van Dijk et al. (33) speculate that a severe, multidecade-long cooling anomaly at 5,100 y BP occurred in the Northern Hemisphere that was potentially forced by sustained high-latitude volcanic eruptions, likely in Iceland. However, the severity of the cooling event at 5,100 y BP possibly was overestimated in the Bader et al. (40) simulation, both globally and for North America, since volcanic sulfate forcings within the model were based on the Greenland Ice Sheet Project 2 (GISP 2) sulfate record, which may have been overly influenced by Icelandic volcanic emissions. For our study, we therefore employed another MPI-ESM simulation (28, 29) to compare forced temperature changes estimated for the Greater Yellowstone Ecosystem with our tree-ring reconstructed high-elevation temperature records (Fig. 5 *B*–*D*). This simulation uses the same model as Bader et al. (40) but with an improved stratospheric aerosol forcing reconstruction based on synchronized bipolar ice-core sulfate records (35).

Direct comparison of the tree-ring reconstructed warm-season (May–Oct) average temperature when scaled against the modeled summer (Jun-Aug) regional average temperature record shows striking agreement in low-frequency temperature variability, with the prediction error of the reconstruction capturing the range of modeled interannual variability (Fig. 5*B*). Differing magnitudes in the simulated-versus-reconstructed temperature decline and variance primarily reflect a difference in seasonal-window length. Only the summer months (Jun-Aug) were averaged together in the simulation data, whereas the six-month warm-season mean (May–Oct) of the reconstruction includes the influence of the cooler shoulder season months. The simulated summer-season mean was used along with the winter season and annual mean for comparison against the warm-season reconstruction to identify the primary seasonal driver underlying the cooling trend. With declining summer insolation in the mid- to late-Holocene, the core summer months of Jun-Aug cooled more rapidly than months in the shoulder seasons, while concurrently winter months were warming. Hence, the differing magnitudes of the simulated and reconstructed temperature declines shown in Fig. 5 are physically supported. Furthermore, the records show a general inverse relationship between stratospheric aerosol optical depth (AOD) and reconstructed and modeled temperature variability (Fig. 5 *B* and *C*), thus indicating that persistent multicentennial cooling anomalies were related to volcanic sulfur emissions (33). Most notably, the sustained 200-y-long regional summer cooling anomaly of 0.8 °C (0.4 °C warm-season reconstructed) that began at c. 5,600 y BP coincided with a decline in the number of living trees and a termination of tree growth at the ice patch (TOL). This cooling anomaly was followed by the prolonged ~68-y-long "Leitahraun" sulfate injection (35) at c. 5,100 y BP that resulted in a nearly century-long 1 °C regional summer cooling anomaly in the simulation. This volcanic cooling event does not correspond directly to tree mortality at the ice patch (TOL), but together with declining summer insolation through the mid- and late Holocene, it suggests that relatively rapid regional cooling allowed for greater accumulation and persistence of snow and ice, which in turn suppressed tree regeneration and led to high-quality wood preservation.

The mid-Holocene upslope expansion of treeline at the ice patches (TOL and TL1) was preceded (before 6,500 y BP) by an insolation-driven summer warming of 1.0 °C and a period of lower treeline elevation in the early Holocene at the nearby TL1 site (Fig. 5 *A* and *D*) (21, 22). The timing of the subsequent upslope shift in treeline in the Greater Yellowstone Ecosystem is not well constrained. The mid-Holocene treeline expansion captured in the ice-patch records generally coincides with that recorded for bristlecone pine in the southwestern United States, though the maximum mid-Holocene treeline elevation captured by the ice patches (TOL and TL1) in the Greater Yellowstone Ecosystem occurred about 1,000 y earlier (30, 31). Pollen records from comparable elevations on the Beartooth Plateau suggest that an expansion of subalpine parkland forest into tundra-steppe vegetation began at some point during the early Holocene insolation-driven warming (21, 43). Thus, the forest structure, demography, and record of growth preserved in the ice patch (TOL; *SI Appendix*, Text S1) likely represents the end of a long period (i.e., several centuries to millennia) of forest expansion. This final record of forest expansion at high elevations on the Beartooth Plateau coincides with the rapid growth of the ice patches (TOL and TL1) (Fig. 5 *A* and *D*), although it is possible that small stands of trees persisted for millennia after the ice patches became established (43).

The amplification of the seasonal cycle of insolation in the early Holocene (prior to 6,500 y BP) had a strong influence on upper treeline across the Greater Yellowstone Ecosystem (43, 44). At this time, summer temperatures were >1 °C above mid-Holocene conditions (as estimated by the climate model, Fig. 5*D*) and winter conditions were colder than present (as evidenced in the TL1 ice-patch $\delta^{18}O$ isotope record (22)). Though the timing and spatial extent is uncertain, the combination of summer aridity and cold winters may have reduced plant-available moisture and led to a lowering of treeline elevation as suggested by pollen records at the TL1 ice patch. Tree establishment at c. 5,900 y BP at the TOL ice-patch site and high levels of subalpine tree pollen at TL1 coincide with a period of anomalous winter warmth and insolation-driven summer cooling relative to the early-Holocene conditions shown in the simulation. During this period, treeline elevations at the ice patches (TOL and TL1) are estimated to be a minimum of ~150 to 180 m above modern treeline. This shift corresponds to a simulated regional summer warming of 2.6 °C (or 0.6 °C annual) during the mid-Holocene (c. 6,500–5,500 y BP) relative to cool conditions during the past millennia (c.1,100–100 y BP) that reduced modern treeline elevations (Fig. 5 *A* and *D*).

Following the mid-Holocene treeline high-stand at the ice patches (TOL and TL1), between 3,930 and 3,560 y BP, the TL1 ice-accumulation rate and $\delta^{18}O$ isotope records (22) provide evidence of persistent and severe cool, wet winter conditions that coincided with the sustained insolation-driven summer cooling trend shown in the model simulation (Fig. 5*D*). This cooling caused continuous freeze-over of the TL1 meltwater pond (21), increases in nearby lake levels (45) and sedimentation rates (46), regional glacier advances (39), and a rapid decrease in regional human population size (47). Regional anomalies in summer average temperature at this time (c. 4,000 to 3,500 y BP) were below −1 °C in the simulation, translating to warm-season temperatures at the TOL ice patch below 5.8 °C. Low temperatures persisted through the Medieval Climate Anomaly (MCA; c. 1,100–500 y BP) until recent decades (Figs. 4*A* and 5 *A* and *D*). This millennial-scale cooling trend was interrupted by a minor summer warming anomaly during the MCA that either caused a modest upslope shift in treeline elevation or simply sustained treeline elevations higher than those of the Little Ice Age (LIA; c. 500–100 y BP).

During the subsequent LIA, the coldest summer temperatures of the Holocene further suppressed treeline to near-modern elevations (43, 48).

Recent Warming and Modern Treeline and Ice Dynamics. Exceptional warming over the past half-century has increased the growth, density, and distribution of subalpine forests in the Greater Yellowstone Ecosystem (Fig. 4 and *SI Appendix*, Figs. S14 and S15) (48) and in high-elevation regions throughout the world (15, 37). The early-to-mid-20th-century temperature estimates for the ice patch (TOL) fall within the range of mid-Holocene average temperatures that were conducive for ice persistence and growth. In contrast, warmer temperatures in recent decades have favored ice loss and upslope forest expansion (Figs. 4 and 5). Relative to the LIA and early-20th century (c. 1900–1950 CE), the first decades of the 21st century are estimated to be >1.2 °C warmer across all seasons at the ice patch (TOL). Moreover, the upper quartile (75%) of the estimated average temperature range at the ice patch today is nearly equivalent to the average 20th-century temperatures associated with modern treeline elevation, while the lower quartile (25%) no longer bounds temperatures that would support ice persistence. Though ice patches are relatively resilient to melt due to the insulative properties of deep and persistent overlying snowpack, the magnitude of recent warming is conducive to rapid melting of ice and treeline expansion throughout the Greater Yellowstone Ecosystem (Figs. 4 and 5*D*). Indeed, 21st-century warming in the Greater Yellowstone Ecosystem and globally has led to rapid melting of ice patches (25) and glaciers (39), and future projections of continued and rapid regional warming (49) suggest the likelihood of near-term and complete melt-out of the TOL ice patch (and many others within the region). Conditions at the ice-patch site (TOL) may once again become suitable for tree establishment if precipitation and plant-available moisture remain adequate. Alternatively, if continued rapid warming results in increased aridity (from reduced precipitation and/or enhanced evapotranspiration) and ecological disturbances (e.g., fire, insect infestation, disease) treeline may be depressed in elevation as it was during the early Holocene. Thus, the future magnitude of warming may lead to two divergent high-elevation scenarios: one in which treeline expands upslope with moderate warming and the other in which it shifts downslope due to increased aridity and disturbance from severe warming. Each carries implications for possible future high-elevation hydrologic conditions and water resources.

Conclusions

Mid-Holocene treeline expansion may have reached its maximum extent in the Greater Yellowstone Ecosystem between 6,500 and 5,500 y BP when ice patch records (TOL and TL1) suggest an elevational increase of at least ~180 m above modern treeline. Other paleobotanical records indicate the forests preserved in the ice patch (TOL) likely represent the end of a long period of forest expansion on the Beartooth Plateau that began during the summer insolation maximum of the early Holocene. It is not currently possible to determine the exact timing of early to mid-Holocene forest expansion or the details of the forest structure (e.g., density, structural continuity, patchiness) during this period, as it is inferred from pollen and plant macrofossil data (21, 43). Our data show that a combination of cooler summers (Fig. 5) and warmer winters (22) in the mid-Holocene allowed forest establishment at the ice-patch site. Increased plant-available moisture at this time facilitated tree growth and recruitment and cooler summer temperatures also maintained steady ice-patch growth across the high elevations of the Greater Yellowstone Ecosystem (21, 43). Decreased summer insolation later in the mid-Holocene and increased sulfur emissions from volcanism at c. 5,600 y BP likely played an important role in a 200-y-long cool period in which summer temperatures decreased by 0.8 °C (or 0.4 °C warm-season reconstructed). Warm-season average temperatures at treeline fell below ~5.8 °C and resulted in a lack of tree growth and establishment and stand-level tree mortality at the ice patch (TOL). A transient global climate model simulation suggests that within a few centuries of the initial cooling event, the 68-y-long "Leitahraun" sulfur injection at c. 5,100 y BP forced a near century-long 1.0 °C regional summer cooling anomaly. This cooling hastened ice-patch growth, prevented tree reestablishment, and preserved dead trees in rapidly forming ice. Continued reduction in summer insolation during the late Holocene (c. 4,000 y BP to present) resulted in a summer cooling of 2.6 °C (or 0.6 °C annual) below mid-Holocene (c. 6,500–5,500 y BP) conditions. This cooling was greatest during the LIA and led to rapid growth of ice patches and glaciers and the maximum treeline suppression of the Holocene across the Greater Yellowstone Ecosystem. Recent warm-season temperatures ≥6.5 °C at the ice patch (TOL) represent a warming of more than 1.2 °C relative to early-20th-century conditions, and temperatures now equal or exceed the estimated mid-Holocene warm-season temperatures when the ice-patch forest stand was present and ice cover was greatly reduced (Figs. 4 and 5*D*). Ice patches and glaciers across the Greater Yellowstone Ecosystem are shrinking, and with continued warming in the coming decades, most will disappear along with the paleoarchives they preserve. Treeline elevation may rise again across the high elevations; however, the current rate and magnitude of projected future warming may also limit moisture and increase ecological disturbances that ultimately restrict future treeline expansion.

Materials and Methods

Modern and Subfossil Whitebark Pine Chronology Development. Cross-sectional samples were extracted from 28 intact subfossil whitebark pine stems melting out of the margin of the TOL ice patch (Fig. 1). At the adjacent modern whitebark pine treeline site (TAL), we extracted increment cores from living trees of similar diameter (>25 cm) and upright growth form (i.e., non-krummholz) to the subfossil logs recovered from the ice patch. Cross-sections and increment core samples were mounted and sanded to a fine polish to expose the anatomy of each annual growth ring. All samples were examined using a binocular microscope and classic visual and statistical dendrochronological methods were used to cross-date the tree-rings for both the subfossil ice-patch and modern-treeline site collections (50, 51). The tree-rings were measured using a sliding stage micrometer with a precision of 0.001 mm, and the dating quality was statistically verified using the "*dplR*" package (version 1.7.2) (52) in the statistical program R (version 4.0.5) (53).

The cross-dated growth chronology for the floating subfossil ice-patch (TOL) record was then anchored in time using radiocarbon dates from 11 annual rings sampled from different trees that spanned the duration of the record (Fig. 2 and *SI Appendix*, Table S2). The samples were submitted to the National Ocean Sciences Accelerator Mass Spectrometry Lab (NOSAMS) at the Woods Hole Oceanographic Institution for ^{14}C radiocarbon dating. The individual rings were then jointly radiocarbon dated using the dated growth year of the sampled ring within the chronology and each sample's measured ^{14}C value and the associated uncertainty (Fig. 2*A*). The calibration was performed using the "IntCal20" (36) curve using the Bayesian radiocarbon chronology package "*Bchron*" in R (54, 55). The calibrated age probability density functions of each sample were generated by randomly calibrating the ^{14}C date and uncertainty range 10,000 times against the IntCal20 curve. The median calibrated age for each sample was then regressed against the dated growth year assigned to each sampled individual growth ring to estimate the calendar year range and dating error of the floating ring-width chronology (Fig. 2*B*). This regression procedure effectively leveraged all the radiocarbon dates to produce a more precise age than any one

radiocarbon date can offer by fixing the number of years in both directions from that best constrained mid-point. We provide the Rms-error (RMSE) from the regression as a conservative estimate of the chronologies dating uncertainty, though the actual dating error range is likely smaller. Calibrated ages are presented in years B.P. (0 y BP = 1,950 CE) and are provided in the publicly available datasets (56) (https://doi.org/10.5066/P147TVZU) in the Georgian calendar notation of year BCE–as estimated without inclusion of a year 0.

To assess growth-climate relationships for both the ice-patch (TOL) and modern treeline (TAL) collections, we utilized the unstandardized (raw) ring-width measurements as well as a standardized, unitless ring-width index (std). For the raw ring-width chronology, each tree-ring measurement series was individually edited using a similar approach as described in Salzer et al. (30) to remove the juvenile biological growth curve, along with any obvious ecological disturbance registered in the tree-rings to produce a quality-controlled measurement series. This functionally removed the majority of the nonclimatic growth factors (including the geometric growth decline) and enabled us to avoid detrending and transforming the raw ring-width data into unitless indices, preserving the measurement values (mm units) for each tree-ring series. This step was critical for the construction of growth-climate transfer functions (described below), since preservation of the mean and distribution of the unstandardized growth measurements is required to capture potential mean changes in reconstructed climate based on the ice-patch wood record. As an initial check to evaluate the dominant climate-growth limitations were common between the raw ring-width records (i.e., had not switched from temperature limited to moisture limited), we then compared the growth and spectral characteristics using partial autocorrelation coefficients and wavelet analysis (57, 58).

To evaluate the quality of the retained climate signal in the modern treeline (TAL) raw tree-ring chronology, a conservatively detrended version of the record was produced for use in monthly and seasonal correlation analyses. We conservatively detrended each series by fitting either a negative exponential curve, negative regression, or mean line (59, 60). The resultant series were then standardized by dividing by the fitted trend line, transformed into unitless ratio (index), and then combined into a composite chronology by calculating the weighted mean across all samples (61). We computed the average raw and standardized ring-width chronologies using the "*dplR*" package (62), and in both chronologies, only the period of record where the express population signal (EPS) remains above 0.85 was retained, limiting additional error attributable to decreasing sample number through time to <15% (63).

Growth-Climate Analyses and Mid-Holocene Temperature Reconstruction. Climate data for the study sites covering the period of 1900–2018 were obtained from the Parameter-elevation Regressions on Independent Slopes Model (PRISM) at 4 km^2 spatial resolution using the AN81m version of the dataset (64). Point estimates of surface temperature and precipitation at the locations of the ice-patch and modern-treeline sites were generated using inverse-distance squared weighting from surrounding grid points for each site elevation. Basin-scale and individual station snow water equivalence (SWE) data were obtained from observational records collected by the Natural Resource Conservation Service's SNOTEL stations and snow-course sites (65) located within the basin, as well as from previous hydrologic unit code 6 (HUC6) watershed analyses performed for the region (66–68).

The potential climate variables (i.e., average temperature, accumulated snowpack, total precipitation) and seasons selected for growth-climate analysis and potential reconstruction were identified using the modern treeline (TAL) whitebark pine chronology (Fig. 1). We used the "*seascorr*" function in the "*treeclim*" (69) and "*dendroTools*" (70, 71) R software packages, as well as nonparametric Spearman rank correlation and regression analyses, to investigate seasonal relationships between tree growth (both raw mm ring-widths and the standardized ring-width index), total precipitation (mm), temperature (°C), and snowpack (measured as April 1 SWE). The "*seascorr*" function was used to identify periods of time within 6-, 12-, and 24-mo windows exhibiting the strongest relationships between modern tree growth and each climate metric. Within this function, nonparametric partial correlation analysis was used to assess the significance of a primary climate variable (e.g., temperature) within the context of secondary, often colinear, climate variables (e.g., precipitation, snowpack) to identify the dominant growth-climate response. We identified warm-season average temperature as the primary growth-climate response and four seasonal target windows for climate reconstruction. The optimal mean temperature seasons identified for reconstruction were 1) warm season (current May–Oct), 2) annual (current Jan–Dec), 3) optimized annual (prior Mar to Jan), and 4) biennial (prior Jan to Oct) (*SI Appendix*, Fig. S8).

Following methods similar to Csank et al. (72, 73) to infer past climate conditions from floating subfossil wood chronologies, we constructed transfer functions to reconstruct past temperature from the ice-patch (TOL) chronology using the contemporary relationship between tree growth and temperature across the four optimized seasonal windows. We developed linear (MLR) and nonlinear (BRNN) transfer functions since the subfossil chronology exhibits slower growth and reduced variability relative to the modern treeline (TAL) chronology (*SI Appendix*, Figs. S2 and S9). This implied that predictions of past temperature would be made from one end of the modern temperature-growth distribution (*SI Appendix*, Fig. S2), so the shape of the relationship and prediction quality at the cold end of the distribution needed to be assessed and utilized to bound a range of past temperature estimates. We tested the robustness of our transfer functions, estimated prediction errors, and selected the best seasonal climate reconstruction target with the lowest prediction error across the range of observations and extremes using a boot-strapped k-folds cross-validation method, and a Central–Edge test (70, 71) (*SI Appendix*, Text S3). We then interpret the optimized warm-season to biennial average temperature reconstructions for the mid-Holocene within the context of the TOL and TL1 ice-patch dynamics and ecological changes influencing treeline, as well as other climate model and proxy-based paleoclimatic records for the region. Since the multiyear temperature-growth relationship in these records retains the strongest temperature signal at decadal to multicentennial timescales, we utilized the root-mean-squared-error of prediction (RMSEp) to infer the range of interannual temperature variability around the low-frequency mean changes captured by the reconstruction.

MPI-ESM Transient Holocene Climate Model Simulation. The Holocene climate model simulation used here was documented in detail by Dallmeyer et al. (34) and the effect of volcanic forcing on Northern Hemisphere climate variations was described in van Dijk et al. (33). It was performed with the MPI-ESM1.2 model (74), which consists of the ocean general circulation model MPIOM (75), including the ocean biogeochemistry model HAMOCC (76), coupled to the atmospheric general circulation model ECHAM6.3 (77). The terrestrial carbon cycle and vegetation dynamics are simulated by JSBACH3 (78) incorporating a dynamic vegetation module developed by Brovkin et al. (79). ECHAM6 and the land model were configured with a spectral resolution of T63 (corresponding to a horizontal resolution of approximately 200 km on a Gaussian grid) with 47 levels in the vertical atmosphere. The ocean model was configured with the horizontal resolution GR15 (corresponding to a horizontal resolution of 12 to 180Â km, and 40 vertical levels). The transient Holocene simulation was branched from a spin-up simulation of over 1,000 y, performed with all forcings fixed to the values of the year 6000Â BCE. The transient simulation then started from this equilibrium state and continued until 1,850 CE.

The transient Holocene simulation included prescribed time-varying forcing agents (34), including 1) orbital-induced insolation changes, 2) greenhouse gas concentrations inferred from ice-core records, 3) stratospheric sulfate aerosols from volcanic eruptions, 4) total and spectral solar irradiance forcing, and 5) changes in land use (only for 800–1,850 CE). The volcanic forcing reconstruction was updated compared to that used in the transient simulation of Bader et al. (40), by incorporating synchronized ice core sulfate data from both Antarctica and Greenland, as described by Sigl et al. (35). Uncertainties in the aerosol forcing for individual eruptions are substantial, but forcing variations on centennial time scales are expected to be more robust as the random uncertainties for individual eruptions average out when multiple eruptions are added together (80). Based on the WD2014 chronology, dating uncertainty for eruptions in the reconstruction is estimated to be 0.5%, corresponding to ±25 y at 5,000 y BP, although dendrochronological evidence suggests actual dating errors to be considerably smaller in the mid-Holocene (35).

Data, Materials, and Software Availability. Tabular Digital Data have been deposited in U.S. Geological Survey, ScienceBase-Catalog (56) (https://doi.org/10.5066/P147TVZU).

ACKNOWLEDGMENTS. This project was funded by the U.S. Geological Survey Ecosystems Land Change Science Program and the Alaska Climate Adaptation Science Center, the NSF (Grants BCS-1832486 and 2149482), the Buffalo Bill

Historical Center's Draper Natural History Museum, University of Wyoming's Biodiversity Institute, Prince Albert II of Monaco Foundation–Monaco and USA, Custer Gallatin National Forest (cost share 07-PA-11010800-017) and Shoshone National Forest (cost shares 08-CS-11021400-014 and 09-CS-11021400-001), and the Sulo and Aileen Maki Endowment at the Desert Research Institute. The ancient, noncultural wood was collected under the provisions of Shoshone National Forest ARPA Permit #CFK317 (exp. 12/31/2018). We thank Andy Bunn and Bryan Shuman for review comments that substantially improved this manuscript, along with comments from Jeremy Littell and Steve Gray on early versions of this manuscript. Any use of trade, firm, or product names is for descriptive purposes only and does not imply endorsement by the US Government.

Author affiliations: [a]U.S. Geological Survey, Northern Rocky Mountain Science Center, Bozeman, MT 59715; [b]Department of Earth Sciences, Montana State University, Bozeman, MT 59717; [c]Department of Physics & Engineering Physics, University of Saskatchewan, Saskatoon, CA S7N 5E2; [d]Max-Planck-Institut für Meteorologie, Hamburg 20146, Germany; [e]Department of Sociology & Anthropology, Montana State University, Bozeman, MT 59717; and [f]Division of Hydrologic Science, Desert Research Institute, Reno, NV 89512

1. P. W. Mote, S. Li, D. P. Lettenmaier, M. Xiao, R. Engel, Dramatic declines in snowpack in the western US. *npj Climate and Atmospheric Sci.* **1**, 2 (2018).
2. R. D. Brown, P. W. Mote, The response of northern hemisphere snow cover to a changing climate. *J. Climate* **22**, 2124–2145 (2010).
3. D. R. Rounce *et al.*, Global glacier change in the 21st century: Every increase in temperature matters. *Science* **379**, 78–83 (2023).
4. L. S. Huning, A. AghaKouchak, Mountain snowpack response to different levels of warming. *Proc. Natl. Acad. Sci. U.S.A.* **115**, 10932–10937 (2018).
5. P. E. Higuera, B. N. Shuman, K. D. Wolf, Rocky Mountain subalpine forests now burning more than any time in recent millennia. *Proc. Natl. Acad. Sci. U.S.A.* **118**, e2103135118 (2021).
6. J. T. Abatzoglou, A. P. Williams, Impact of anthropogenic climate change on wildfire across western US forests. *Proc. Natl. Acad. Sci. U.S.A.* **113**, 11770–11775 (2016).
7. K. F. Raffa, E. N. Powell, P. A. Townsend, Temperature-driven range expansion of an irruptive insect heightened by weakly coevolved plant defenses. *Proc. Natl. Acad. Sci. U.S.A.* **110**, 2193–2198 (2013).
8. C. Parmesan, G. Yohe, A globally coherent fingerprint of climate change impacts across natural systems. *Nature* **421**, 37–42 (2003).
9. M. Gottfried *et al.*, Continent-wide response of mountain vegetation to climate change. *Nat. Climate Change* **2**, 111–115 (2012).
10. C. Körner, A re-assessment of high elevation treeline positions and their explanation. *Oecologia* **115**, 445–459 (1998).
11. C. Körner, J. Paulsen, A world-wide study of high altitude treeline temperatures. *J. Biogeography* **31**, 713–732 (2004).
12. C. Körner, *Alpine Treelines* (Springer Basel, 2012).
13. M. A. Harsch, M. Y. Bader, Treeline form–a potential key to understanding treeline dynamics. *Global Ecol. Biogeography* **20**, 582–596 (2011).
14. K. Hermes, "Die Lage der oberen Waldgrenze in den Gebirgen der Erde und ihr Abstand zur Schneegrenze" in *Geographischen Instituts* (Universität Köln, Cologne, Germany, 1955), p. 277.
15. M. A. Harsch, P. E. Hulme, M. S. McGlone, R. P. Duncan, Are treelines advancing? A global meta-analysis of treeline response to climate warming *Ecol. Lett.* **12**, 1040–1049 (2009).
16. A. G. Bunn, L. A. Waggoner, L. J. Graumlich, Topographic mediation of growth in high elevation foxtail pine (Pinus balfouriana Grev. et Balf.) forests in the Sierra Nevada, USA. *Global Ecol. Biogeography* **14**, 103–114 (2005).
17. B. L. Coulthard *et al.*, Snowpack signals in North American tree rings. *Environ. Res. Lett.* **16**, 034037 (2021).
18. R. A. Andrus, B. J. Harvey, K. C. Rodman, S. J. Hart, T. T. Veblen, Moisture availability limits subalpine tree establishment. *Ecology* **99**, 567–575 (2018).
19. A. G. Bunn, M. W. Salzer, K. J. Anchukaitis, J. M. Bruening, M. K. Hughes, Spatiotemporal variability in the climate growth response of high elevation bristlecone pine in the white mountains of California. *Geophys. Res. Lett.* **45**, 13,312–13,321 (2018).
20. N. C. Pepin *et al.*, Climate changes and their elevational patterns in the mountains of the world. *Rev. Geophys.* **60**, e2020RG000730 (2022).
21. M. Alt *et al.*, Organic layers preserved in ice patches: A new record of Holocene environmental change on the Beartooth Plateau, USA. *The Holocene* **34**, 338–352 (2023).
22. N. J. Chellman *et al.*, High elevation ice patch documents Holocene climate variability in the northern Rocky Mountains. *Quaternary Sci. Adv.* **3**, 100021 (2021).
23. C. M. Lee, R. L. Kelly, R. Reckin, I. L. Matt, P.-L. Yu, Ice patch archaeology in Western North America. *SAA Archaeol. Record* **14**, 15–19 (2014).
24. C. M. Lee, K. Puseman, Ice patch hunting in the greater yellowstone area, Rrocky Mountains, USA: Wood shafts, chipped stone projectile points, and bighorn sheep (Ovis Canadensis). *Am. Antiquity* **82**, 223–243 (2017).
25. R. Farnell *et al.*, Multidisciplinary investigations of alpine ice patches in Southwest Yukon, Canada: Paleoenvironmental and paleobiological investigations. *Arctic* **57**, 247–259 (2004).
26. Seifert *et al.*, Monitoring alpine climate change in the Beartooth Mountains of the Custer National Forest. *Forest Service Report*, 1–6 (2009).
27. R. M. Kellogg, S. Rowe, R. C. Koeppen, R. B. Miller, Identification of the Wood of the Soft Pines of Western North America. *IAWA J.* **3**, 95–101 (1982).
28. P. J. van Mantgem *et al.*, Growth, drought response, and climate-associated genomic structure in whitebark pine in the Sierra Nevada of California. *Ecol. Evol.* **13**, e10072 (2023).
29. N. E. Kichas, G. T. Pederson, S. M. Hood, R. G. Everett, D. B. McWethy, Increased whitebark pine (Pinus albicaulis) growth and defense under a warmer and regionally drier climate. *Front. Forests Global Change* **6**, 1089138 (2023).
30. M. W. Salzer, A. G. Bunn, N. E. Graham, M. K. Hughes, Five millennia of paleotemperature from tree-rings in the Great Basin, USA. *Clim. Dyn.* **42**, 1517–1526 (2014).
31. A. G. Bunn, M. K. Hughes, M. W. Salzer, Topographically modified tree-ring chronologies as a potential means to improve paleoclimate inference. *Climatic Change* **105**, 627–634 (2011).
32. M. Salzer, M. Hughes, A. Bunn, K. Kipfmueller, Recent unprecedented tree-ring growth in bristlecone pine at the highest elevations and possible causes. *Proc. Natl. Acad. Sci. U.S.A.* **106**, 20348 (2009).
33. E. van Dijk, J. Jungclaus, M. Sigl, C. Timmreck, K. Kruger, High-frequency climate forcing causes prolonged cold periods in the holocene. *Nat. Commun. Earth & Environ.* **5**, 242 (2024).
34. A. Dallmeyer *et al.*, Holocene vegetation transitions and their climatic drivers in MPI-ESM1.2. *Clim. Past* **17**, 2481–2513 (2021).
35. M. Sigl, M. Toohey, J. R. McConnell, J. Cole-Dai, M. Severi, Volcanic stratospheric sulfur injections and aerosol optical depth during the Holocene (past 11 500 years) from a bipolar ice-core array. *Earth Syst. Sci. Data* **14**, 3167–3196 (2022).
36. P. J. Reimer *et al.*, The IntCal20 Northern Hemisphere radiocarbon age calibration curve (0–55 cal kBP). *Radiocarbon* **62**, 725–757 (2020).
37. K. F. Kipfmueller, M. W. Salzer, Linear trend and climate response of five-needle pines in the western United States related to treeline proximity. *Canadian J. Forest Res.* **40**, 134–142 (2010).
38. P. D. W. Tranquillini, "Physiological ecology of the alpine timberline" in *Ecological Studies* (1979).
39. D. J. Larsen, S. E. Crump, A. Blumm, Alpine glacier resilience and Neoglacial fluctuations linked to Holocene snowfall trends in the western United States. *Sci. Adv.* **6**, eabc7661 (2020).
40. J. Bader *et al.*, Global temperature modes shed light on the Holocene temperature conundrum. *Nat. Commun.* **11**, 4726 (2020).
41. B. N. Shuman, J. Marsicek, The structure of Holocene climate change in mid-latitude North America. *Quaternary Sci. Rev.* **141**, 38–51 (2016).
42. B. N. Shuman, Patterns of centennial to millennial Holocene climate variation in the North American mid-latitudes. *Clim. Past* **20**, 1703–1720 (2024).
43. V. Iglesias, C. Whitlock, T. R. Krause, R. G. Baker, Past vegetation dynamics in the Yellowstone region highlight the vulnerability of mountain systems to climate change. *J. Biogeography* **45**, 1768–1780 (2018).
44. C. Whitlock, P. J. Bartlein, Spatial variations of holocene climatic change in the Yellowstone Region. *Quaternary Res.* **39**, 231–238 (2017).
45. B. N. Shuman, M. Serravezza, Patterns of hydroclimatic change in the Rocky Mountains and surrounding regions since the last glacial maximum. *Quaternary Sci. Rev.* **173**, 58–77 (2017).
46. J. R. Stone, J. E. Saros, G. T. Pederson, Coherent late-Holocene climate-driven shifts in the structure of three Rocky Mountain lakes. *The Holocene* **26**, 1103–1111 (2016).
47. R. L. Kelly, T. A. Surovell, B. N. Shuman, G. M. Smith, A continuous climatic impact on Holocene human population in the Rocky Mountains. *Proc. Natl. Acad. Sci. U.S.A.* **110**, 443–447 (2013).
48. M. L. Rochner, K. J. Heeter, G. L. Harley, M. F. Bekker, S. P. Horn, Climate-induced treeline mortality during the termination of the Little Ice Age in the Greater Yellowstone Ecoregion, USA. *The Holocene* **31**, 1288–1303 (2021).
49. S. Hostetler *et al.*, *Greater Yellowstone Climate Assessment* (Montana State University, Institute on Ecosystems, Bozeman, MT, 2021), pp. 1–218.
50. A. E. Douglass, Crossdating in dendrochronology. *J. Forestry* **39**, 825–831 (1941).
51. M. A. Stokes, T. L. Smiley, *An Introduction to Tree-ring Dating* (University of Arizona Press, 1996).
52. A. G. Bunn, Statistical and visual crossdating in R using the dplR library. *Dendrochronologia* **28**, 251–258 (2010).
53. R Development Core Team, *R: A Language and Environment for Statistical Computing* (R Foundation for Statistical Computing, Vienna, Austria, 2008).
54. J. Haslett, A. Parnell, A simple monotone process with application to radiocarbon-dated depth chronologies. *J. R. Stat. Soc. Series C (Appl. Stat.)* **57**, 399–418 (2008).
55. A. C. Parnell, J. Haslett, J. R. M. Allen, C. E. Buck, B. Huntley, A flexible approach to assessing synchroneity of past events using Bayesian reconstructions of sedimentation history. *Quaternary Sci. Rev.* **27**, 1872–1885 (2008).
56. G. T. Pederson *et al.*, Mid-Holocene-to-present Modeled (ca., 7,000 to 100 cal. BP) and Reconstructed (ca., 5,900 to 5,436 cal. BP) Temperature for the High-Elevations of the Greater Yellowstone Ecosystem: Derived from a Transient Climate Model and Whitebark Pine Tree-rings. U.S. Geological Suvey. https://doi.org/10.5066/P147TVZU. Accessed 16 December 2024.
57. Y. Liu, X. San Liang, R. H. Weisberg, Rectification of the Bias in the Wavelet Power Spectrum. *J. At. Oceanic Technol.* **24**, 2093–2102 (2007).
58. C. Torrence, G. Compo, A practical guide to wavelet analysis. *Bull. Am. Meteorol. Soc.* **79**, 61–78 (1998).
59. H. C. Fritts, *Tree Rings and Climate* (Academic Press, New York, N.Y., 1976), p. 553.
60. E. R. Cook *et al.* "Tree-ring standardization and grow-trend estimation" in *Methods of Dendrochonology: Applications in the Environmental Sciences*. (1990), pp. 104–123.
61. E. R. Cook, K. Peters, Calculating unbiased tree-ring indices for the study of climatic and environmental change. *The Holocene* **7**, 361–370 (1997).
62. A. G. Bunn, A dendrochronology program library in R (dplR). *Dendrochronologia* **26**, 115–124 (2008).
63. T. M. L. Wigley, K. R. Briffa, P. D. Jones, On the average value of correlated time series, with applications in dendroclimatology and hydrometeorology. *J. Climate and Appl. Meteorol.* **23**, 201–213 (1984).
64. C. Daly *et al.*, Physiographically sensitive mapping of climatological temperature and precipitation across the conterminous United States. *Int. J. Climatol.* **28**, 2031–2064 (2008).
65. N. R. C. S. (NRCS), *Snow Telemetry (SNOTEL) and Snow Course Data* (U.S. Department of Agriculture, 2018).
66. G. T. Pederson, J. L. Betancourt, G. J. McCabe, Regional patterns and proximal causes of the recent snowpack decline in the Rocky Mountains, U.S. *Geophys. Res. Lett.* **40**, 1811–1816 (2013).
67. G. T. Pederson *et al.*, The unusual nature of recent snowpack declines in the North American cordillera. *Science* **333**, 332–335 (2011).
68. E. K. Wise, C. A. Woodhouse, G. J. McCabe, G. T. Pederson, J.-M. St-Jacques, Hydroclimatology of the Missouri River Basin. *J. Hydrometeorol.* **19**, 161–182 (2018).

69. C. Zang, F. Biondi, treeclim: An R package for the numerical calibration of proxy-climate relationships. *Ecography* **38**, 431–436 (2014).
70. J. Jevšenak, T. Levanič, dendroTools: R package for studying linear and nonlinear responses between tree-rings and daily environmental data. *Dendrochronologia* **48**, 32–39 (2018).
71. J. Jevšenak, T. Levanič, S. Džeroski, Comparison of an optimal regression method for climate reconstruction with the compare_methods() function from the dendroTools R package. *Dendrochronologia* **52**, 96–104 (2018).
72. A. Z. Csank, D. Fortier, S. W. Leavitt, Annually resolved temperature reconstructions from a late Pliocene–early Pleistocene polar forest on Bylot Island, Canada. *Palaeogeogr. Palaeoclimatol. Palaeoecol.* **369**, 313–322 (2013).
73. A. Z. Csank, W. P. Patterson, B. M. Eglington, N. Rybczynski, J. F. Basinger, Climate variability in the Early Pliocene Arctic: Annually resolved evidence from stable isotope values of sub-fossil wood, Ellesmere Island, Canada. *Palaeogeography, Palaeoclimatology, Palaeoecology* **308**, 339–349 (2011).
74. T. Mauritsen *et al.*, Developments in the MPI-M earth system model version 1.2 (MPI-ESM1.2) and its response to increasing CO(2). *J. Adv. Model Earth Syst* **11**, 998–1038 (2019).
75. J. H. Jungclaus *et al.*, Characteristics of the ocean simulations in the Max Planck Institute Ocean Model (MPIOM) the ocean component of the MPI-Earth system model. *J. Adv. Model. Earth Syst.* **5**, 422–446 (2013).
76. T. Ilyina *et al.*, Global ocean biogeochemistry model HAMOCC: Model architecture and performance as component of the MPI-Earth system model in different CMIP5 experimental realizations. *J. Adv. Model. Earth Syst.* **5**, 287–315 (2013).
77. B. Stevens *et al.*, Atmospheric component of the MPI-M earth system model: ECHAM6. *J. Adv. Model. Earth Syst.* **5**, 146–172 (2013).
78. C. H. Reick, T. Raddatz, V. Brovkin, V. Gayler, Representation of natural and anthropogenic land cover change in MPI-ESM. *J. Adv. Model. Earth Syst.* **5**, 459–482 (2013).
79. V. Brovkin, T. Raddatz, C. H. Reick, M. Claussen, V. Gayler, Global biogeophysical interactions between forest and climate. *Geophys. Res. Lett.* **36**, L07405 (2009).
80. J. C. Schindlbeck-Belo, M. Toohey, M. Jegen, S. Kutterolf, K. Rehfeld, PalVol v1: A proxy-based semi-stochastic ensemble reconstruction of volcanic stratospheric sulfur injection for the last glacial cycle (140 000–50 BP). *Earth Syst. Sci. Data* **16**, 1063–1081 (2024).